1 # Revision_1

2,3 # A neutron diffraction study of the hydrous borate inderborite, $CaMg[B_3O_3(OH)_5]_2(H_2O)_4 \cdot 2H_2O$

4 G. Diego Gatta, Enrico Cannaò, Davide Comboni,

5 Tommaso Battiston and Oscar Fabelo

6

7 **Running title:** Crystal chemistry of inderborite

8

20

21

22 **Corresponding author: G. Diego GATTA**

23 Dipartimento di Scienze della Terra, Università degli Studi di Milano

24 Via Botticelli 23, I-20133 Milano, Italy

25 Tel. +39 02 503 15607, Fax +39 02 503 15597, E-Mail: diego.gatta@unimi.it

26

27

28

29 *Manuscript submitted to American Mineralogist*

1

A neutron diffraction study of the hydrous borate inderborite, $CaMg[B_3O_3(OH)_5]_2(H_2O)_4 \cdot 2H_2O$

G. Diego Gatta[1], Enrico Cannaò[1], Davide Comboni[1],

Tommaso Battiston[1] and Oscar Fabelo[2]

[1]Dipartimento di Scienze della Terra, Università degli Studi di Milano,
Via Botticelli 23, I-20133 Milano, Italy
[2]Institut Laue-Langevin, 71 Avenue des Martyrs, F-38000 Grenoble, France

Abstract

The crystal chemistry of inderborite, a B-rich mineral ($B_2O_3 \sim 41$ wt%) with ideal formula $CaMg[B_3O_3(OH)_5]_2 \cdot 6H_2O$ or $CaMg[B_3O_3(OH)_5]_2(H_2O)_4 \cdot 2H_2O$ from the Inder Deposit, Kazakhstan, was re-investigated by a multi-methodological approach (single-crystal X-ray and neutron diffraction, electron probe micro-analysis in wavelength dispersive mode, laser ablation- multi collector inductively mass spectrometry). The experimental findings show that the real chemical formula of inderborite from the Inder Deposit is virtually identical to the ideal one: the fraction of potential isomorphic substituents is substantially insignificant. Boron is, therefore, the only industrially-relevant element occurring in this mineral. The *in-situ* B isotope composition of the Inder inderborite shows enrichment in the heavy ^{11}B isotope, giving a weighted mean $\delta^{11}B_{NIST951}$ of $+35.15 \pm 0.49$ ‰ (2σ, N = 6). Such a positive $\delta^{11}B$ value falls within the range of values in which the source of boron is ascribable to marine reservoirs, rather than to terrestrial ones.

X-ray (at 293 K) and neutron (at 20 K) structure refinements confirm that the principal building block unit of the structure is a $[B_3O_3(OH)_5]^{2-}$ ring, consisting of two $BO_2(OH)_2$ tetrahedra (B-ion in sp^3 electronic configuration) and one planar-triangular BO_2OH group (B-ion in sp^2 electronic configuration). In the $[B_3O_3(OH)_5]^{2-}$ ring, all the oxygen atoms that are not shared between two boron atoms are protonated. The building units share corners with the $CaO_2(OH)_4(OH_2)_2$ polyhedra and $Mg(OH)_4(OH_2)_2$ octahedra, forming hetero-polyhedral sheets parallel to (100). Subsequent hetero-polyhedral sheets are mutually connected only by H-bonding interactions, even mediated by the zeolitic ("interstitial") H_2O molecules. Ten over eleven independent oxygen sites in the structure of inderborite are involved in H-bonds as *donor* or *acceptors*, and this reflects the pervasive effect of the H-bonding network. The role played by the complex H-bond network is expected to be substantial on the stability of the crystalline edifice, having effects within the single hetero-polyhedral sheet, between subsequent sheets, and to bond the interstitial zeolitic H_2O molecules.

The potential utilizations of inderborite, as a B-bearing mineral, are discussed.

64   **Keywords:** Inderborite, borates, mineral commodity, X-ray diffraction, neutron diffraction, crystal

65   chemistry, hydrogen bonding.

66

67   **Introduction**

68   Inderborite is an hydrous borate, with ideal chemical formula $CaMg[B_3O_3(OH)_5]_2 \cdot 6H_2O$, found

69   in lacustrine borate deposits or in the caprock of salt diapers, usually coexisting with other common

70   borates, as borax $(Na_2[B_4O_5(OH)_4] \cdot 8H_2O)$, ulexite $(NaCa[B_5O_6(OH)_6] \cdot 5H_2O)$, colemanite

71     $(Ca[B_3O_4(OH)_3] \cdot H_2O)$, hydroboracite $(CaMg[B_3O_4(OH)_3]_2 \cdot 3H_2O)$, kurnakovite

72     $(MgB_3O_3(OH)_5 \cdot 5H_2O)$, inderite $(MgB_3O_3(OH)_5 \cdot 5H_2O)$, and pinnoite $(Mg[B_2O(OH)_6]$. The type locality

73   of this mineral is the Inder borate deposit, Kazakhstan. Inderite contains boron as an essential component

74   (more than 41 wt% B_2O_3) and, along with the other hydrous borates from lacustrine deposits, they

75   represent more than 90% of the B-rearing minerals utilised by industry worldwide. The worldwide

76   request of borates has drastically increased the last 20 years, and the market is expected to grow in the

77   near future, in order to accommodate the raising demand of B in a series of technologically relevant

78   products (*e.g.*, ceramics and refractory materials, heat-resistant glasses, fire retardants, radiation-

79   shielding materials, B-alloy steels, pharmaceutical products, soaps and detergents, and agricultural

80   compounds) (source: U.S.G.S. Mineral Commodity Summaries, https://www.usgs.gov/centers/national-

81   minerals-information-center/mineral-commodity-summaries; British Geological Survey – Centre for

82   Sustainable Mineral Development, https://www2.bgs.ac.uk/mineralsuk). Due to its high supply risk and

83   economic importance, boron is among the critical elements, included in the "critical raw materials" list

84   according to the European Commission 2023

85   (https://ec.europa.eu/commission/presscorner/detail/en/ip_23_1661).

86   In the last years, we have re-investigated the crystal structure and physical and chemical stability (at

87   high/low temperature and high pressure conditions, or in response to leaching) of a series of borates:

88   colemanite (Lotti et al. 2017, 2018, 2019), kurnakovite (Gatta et al. 2019; Pagliaro et al. 2021), kernite

89     $(Na_2B_4O_6(OH)_2 \cdot 3H_2O$, Comboni et al. 2020a; Gatta et al. 2020), meyerhofferite

90     $(Ca_2[B_6O_6(OH)_{10}] \cdot 2H_2O$, Comboni et al. 2020b, Gatta et al. 2022a), inyoite $(CaB_3O_3(OH)_5 \cdot 4H_2O$,

91   Comboni 2022), probertite $(CaNa[B_5O_7(OH)_4] \cdot 3H_2O$, Gatta et al. 2022b), and inderite (Comboni et

92   al. 2023) by a multi-methodological approach. Our experiments were aimed to search for potential B-

93   rich aggregates in construction materials (*e.g.*, Portland or Sorel cements), due to the efficient radiation-

94   shielding capacity of ^{10}B (its high cross section for the $^{10}B(n,\alpha)^7Li$ reaction is ~3840 barns; Carter et al.

95   1953, Sears 1986, Palmer and Swihart 1996, Rauch and Waschkowski 2002). The neutron absorption

96   capacity of ^{11}B is, on the other hand, modest (cross section ~0.006 barns), but in natural borates about

3

97   20% of boron occurs as [10]B. Following the previous experiments, the aim of this paper is to extend our

98   systematic study on borates to inderborite, among the natural borates with the highest B-content (~41

99   wt% B_2O_3). Here, we report the experimental findings based on single-crystal X-ray (at 298 K) and

100   neutron diffraction (at 20 K), electron microprobe analysis in wavelength-dispersive mode (EPMA-

101   WDS), and laser ablation - inductively mass spectrometry (LA-ICP-MS) and LA- multi collectors

102   ICP-MS (LA-MC-ICP-MS), providing: 1) the chemical composition of this mineral (unveiling major,

103   minor and trace elements), and its B isotopic composition, and 2) a structural model based on modern

104   standards, with the location of all the H sites, their vibrational regime and the description of the complex

105   and pervasive H-bonding net (inderborite contains up to ~39 wt% of total H_2O), which is presumed to

106   cover a substantial role on the thermal and compressional stability of this mineral (currently under

107   investigation), limiting its potential use as B-aggregate in concretes. Due to the high B and H content,

108   and the occurrence of millimetric gem-quality crystals, inderborite is a good candidate for a neutron

109   diffraction investigation.

110

111   **Previous studies on inderborite**

112   Inderborite was discovered, as a new mineral species, by Gorshkov (1941) at the Lower Permian

113   gypsum beds in the Inder mountains, northwards from lake Inder, Guriev region, Kazakhstan, in

114   paragenesis with other already known (at that time) hydrous borates: colemanite, ulexite and inyoite.

115   The first crystallographic data collected by Gorshkov (1941) suggested that the mineral were monoclinic

116   (with a ratio among unit-cell edges of $a : b : c$ = 1.6346 : 1 : 1.3173 and a monoclinic angle of β =

117   90°48'), and the first (wet) chemical characterization led to the ideal formula $CaO \cdot MgO \cdot 3B_2O_3 \cdot 11H_2O$

118   (or $CaMgB_6O_{11} \cdot 11H_2O$). Independently, but slightly later in the same year, even Ikornikova and

119   Godevlsky (1941) reported the finding of a new mineral species (proposed name: metahydroboracite),

120   but their chemical and crystallographic data were virtually identical to those previously reported by

121   Gorshkov (1941) for inderborite. The name assigned to the new mineral was, therefore, inderborite

122   (Fleischer 1943). Later, the crystal structure of inderborite, from the type locality in Kazakhstan, was

123   solved and refined by Kurkutova et al. (1966), on the basis of two-dimensional photographic X-ray

124   single-crystal data. The structure model was described in the space group $C2/c$ and, despite consistent at

125   a first approximation, was provided without any H sites and with a poor agreement factor (R-factor). A

126   better model was later provided by Burns and Hawthorne (1994), on the basis of a high-quality single-

127   crystal X-ray structure refinement, with a first assignment of eleven independent H sites. The space group

128   was confirmed to be $C2/c$, with unit-cell parameters a~12.137, b~7.433, c~19.234 Å, and β~90.3°, and

129   the crystallographically-derived chemical formula was given as: $CaMg[B_3O_3(OH)_5]_2(H_2O)_4 \cdot 2H_2O$

4

130 (*Z*=4). The principal building block unit of the inderborite structure (also called "fundamental building

131 block" unit by Burns and Hawthorne, 1994) is a $[B_3O_3(OH)_5]^{2-}$ ring, consisting of two B-tetrahedra and

132 one planar-triangular B-unit (Fig. 1). The same building block unit occurs also in the structure of

133 kurnakovite, meyerhofferite, inyoite, inderite and solongoite (Hawthorne 2012). In the $[B_3O_3(OH)_5]^{2-}$

134 ring, all the oxygen atoms that are not shared between two boron atoms are protonated (Burns and

135 Hawthorne 1994). In inderborite, the building units share corners with the Ca-polyhedra and Mg-

136 octahedra, forming hetero-polyhedral sheets parallel to (100), as shown in Fig. 1. The role played by the

137 complex H-bond network was expected to be substantial, having effects within the single building unit,

138 between adjacent units, and to bond the zeolitic H_2O molecules.

139   Despite the structure model of inderborite has been essentially unveiled, it is surprising that, in

140 the literature, there is no data, based on modern standards, about the chemical composition of this

141 mineral, especially for minor and trace elements. To date, nature and role of potential substituents for

142 Ca, Mg, B and OH-group are completely unknown.

143

144   **Materials and Experimental methods**

145   -   *Inderborite sample*

146   The sample of inderborite investigated in this study was kindly provided by the late Dr. Renato

147 Pagano (Italy), with ref. #8029 of his collection. The hand specimen is represented by some

148 colourless, well-formed prismatic, millimetric crystals from the "Quarry 98", Inder Deposit,

149 Kazakhstan, in which inderborite coexists with other borates (*e.g.,* borax, boracite, colemanite,

150 inderite, inyoite, kurnakovite, pinnoite, preobrazhenskite, tyretskite, ulexite, volkovskite), sulphates

151 (*e.g.*, anhydrite, celestine, gypsum, thénardite, vanthoffite), halides-fluorides, carbonates (*e.g.*,

152 aragonite, calcite, dolomite), and silicates (mainly clay minerals). The borates at the Inder deposit are

153 geologically connected to a Permian salt dome that intrudes Mesozoic and Cenozoic sediments,

154 covering an area of about 100 sq. miles. Halides, sulphates and clay minerals form the internal part

155 of the salt dome, whereas the external part consists of a series of Permian gypsum-rich rocks, with

156 reddish clays interbedded with borates ores. A detailed description of the Inder deposit is provided

157 by Pekov and Abramov (1993) and Pekov (1998).

158

159   -   *Chemical characterization*

160   The chemical composition of the inderborite sample of this study was first investigated by

161 EPMA-WDS with a JEOL 8200 Super Probe system at the Earth Sciences Department, University of

162 Milan (ESD-MI), with the following operating conditions: 15 kV and 5 nA, 5 μm beam diameter, 30

s of counting times on the peaks and 10 s on the backgrounds. A series of minerals was used as standards; the results were corrected for matrix effects using a *ZAF* routine, as implemented in the JEOL suite of programs. The standards employed were: forsterite-154 (Mg), fayalite-143 (Fe), grossular (Al, Si, Ca), K-feldspar (K), omphacite (Na), sanbornite (Ba), celestine (Sr), apatite (F). The three milimetric crystals of inderborite under investigation were found to be homogeneous, but with some micro-inclusions of quartz. Only Ca and Mg concentrations were measured at a significant level. The measured weight fractions of Ca and Mg were nominally identical to the ideal ones (within the *e.s.d.*), *i.e.*, CaO 11.2(2) wt% and MgO 7.9(2) wt%. As commonly observed for hydrous borates (*e.g.*, Gatta et al. 2022b), even in this case a modest degeneration of the crystals was observed under the electron beam.

Trace element concentration was determined using a laser ablation system (Analyte Excite ArF excimer 193 nm, Teledyne Photon Machines) coupled to a single-collector quadrupole ICP-MS (iCAP RQ, Thermo Fisher Scientific) hosted at the Geochemistry, Geochronology and Isotope Geology laboratory of the ESD-MI. The laser microprobe system is equipped with an HelEx II volume chamber for a fast wash out of the ablated materials. Helium was used as carrier gas with a flow rate of ~ 0.5 L/min in the ablation cell and ~ 0.2 L/min in the HelEx II cup. The laser spot size was set to 65 μm and a laser fluence of 2.0 J/cm^2, with a repetition rate of 7 Hz, was used. Each analyses consisted of 40s of background signal, 60s of laser signal and 20s of wash out time. The NIST SRM 610 synthetic glass was used as primary external standard (Jochum et al. 2011) and ^{43}Ca was used as internal standard. Quality control was achieved by analyzing the USGS reference basaltic glass GSD-2g (Wilson 2018), the NIST SRM 612 (Jochum et al. 2011), and the IAEA-B6 obsidian (Tonarini et al. 2003) together with the unknown. Precision is better than 5% for most of the elements and accuracy is within 10% of the reference values. Data reduction was carried out using the Glitter software package (Griffin et al. 2008). Data are listed in Table 1.

The *in-situ* B isotope composition of the Inder inderborite was measured using the same laser ablation system used for the determination of the trace element concentrations, connected with a double focusing multi collector (MC-)ICP-MS (Neptune *XT*, Thermo Fisher Scientific) hosted at the ESD-MI. The measurements were performed in single spot mode with a laser fluence of 3.0 J/cm^2 on the sample surface, a repetition rate of 7 Hz, and a fixed spot size diameter of 40 μm. The He flow rates within the ablation cell and in the arm of the HelEx II were set to ~ 0.51 and ~ 0.24 L/min, respectively. The signal intensity of the ^{11}B and ^{10}B were simultaneously acquired using two Faraday cups (H4 and L2, respectively) connected to 10^{11} Ω amplifier resistors. The instrumentation was setup for maximum sensitivity using 0.8 X-skimmer and 0.8 Ni-Jet sample cones, and the Jet pump at the

6

196   ICP interface. The isobaric interferences of $^{40}Ar^{4+}$ and $^{20}Ne^{2+}$ on mass 10 were resolved working at

197   low-resolution mode. Each analyses consisted of 60 cycles of background followed by 80 cycles of

198   data acquisition, and 16 cycles of wash time, for a total of 156 cycles of ~ 0.5 s each. The results are

199   reported in the common delta(δ)-notation as permil (‰) and expressed relative to the isotopic ratio

200   of the NIST SRM 951 boric acid ($^{11}B/^{10}B$ = 4.04362 ± 0.00137, 2σ; Catanzaro et al. 1970). Data

201   reduction was carried out offline with an *in-house* spread sheet; $^{11}B/^{10}B$ ratios exceeding 2σ have

202   been discharged. No downhole isotope ratio fractionation was observed. Instrumental isotope

203   fractionation was corrected using the sample-standard bracketing approach using the IAEA-B4

204   tourmaline (schorl) as primary standard ($δ^{11}B$ = -8.62 ± 0.17, 2σ; Tonarini et al. 2003). Potential

205   laser-induced isotope fractionation was evaluated analyzing two dravitic tourmalines (SY309 and

206   SY441 from Marschall et al. 2006) and the B-rich synthetic andesitic glass ARM-2 (10500 wt. ppm

207   of B, Wu et al. 2021) in the same analytical run with the Inder inderborite. Boron isotope composition

208   obtained for the dravitic tourmalines ($δ^{11}B_{SY441}$ = +19.41 ± 0.40 ‰, 2σ, N = 2; $δ^{11}B_{SY309}$ = +21.22 ±

209   0.47 ‰, 2σ, N = 2), and for the andesitic ARM-2 glass ($δ^{11}B$ = -11.74 ± 0.52 ‰, 2σ, N = 4) agree

210   with the published values. Further check for potential instrumental and laser-induced isotope

211   fractionation were done by analyzing a new set of tourmaline standards (Schorl 112566, Dravite

212   108796, and Elbaite 98144) in a separate session at similar instrumental parameters and conditions,

213   and using the IAEA-B4 tourmaline as calibrating standard. The measured $δ^{11}B$ values are -13.38 ±

214   0.15 ‰ (2σ, N = 3) for the Schorl 112566, -6.29 ± 0.02 ‰ (2σ, N = 3) for the Dravite 108796, and -

215   12.11 ± 0.05 ‰ (2σ, N = 3) for the Elbaite 98144 and are accurate within uncertainties with published

216   values (Leeman and Tonarini 2001; Mikovà et al. 2014; Marger et al. 2020). The B isotopic

217   composition of the Inder inderborite is given in Table 1.

218

219   -   ***Single-crystal X-ray and neutron diffraction***

220   To assess the quality of a range of crystals varying in size and shape, a KUMA-KM4 four-

221   circle X-ray diffractometer was initially employed. This assessment aimed to select the better crystals

222   for the collection of X-ray and neutron intensity data. Among those, a prismatic crystal (*ca.* 0.08 x

223   0.130 x 0.230 mm^3) of inderborite was selected for the X-ray intensity data collection, at room

224   temperature (*ca*. 293 K), with a Rigaku XtaLABSynergy-i X-ray diffractometer, equipped with a

225   PhotonJet-i Mo*K*α microfocus source and a HyPix-6000HE HPC detector, at the ESD-MI. Diffraction

226   data were collected using an *ad hoc* routine suggested by the *CrysAlisPro™* suite (Rigaku – Oxford

227   Diffraction 2019), maximising the reciprocal space coverage and the quality of the intensity data,

228   adopting an ω-scan strategy, 0.5° step size and an exposure time of 1 s per frame. A total number of

7

229   5759 Bragg reflections was collected up to $2\theta_{max}$ of 60° (with $-15 \leq h \leq +11$, $-9 \leq k \leq +9$ and $-25 \leq l$

230    $\leq +26$), giving a metrically monoclinic unit-cell with: $a = 12.1593(8)$, $b = 7.4084(6)$, $c = 19.230(2)$

231   Å, $\beta = 90.321(9)°$ and $V = 1732.2(3)$ Å^3; 1923 reflections were unique for symmetry ($R_{int} = 0.0248$,

232   Laue class $2/m$) and 1832 with $I_o > 2\sigma(I_o)$. The reflection conditions were consistent with the space

233   group $C2/c$. The intensity data were then corrected for Lorentz-polarization effects and X-ray

234   absorption (with a semi-empirical strategy) using the *ABSPACK* routine, implemented in the

235   *CrysAlisPro^{TM}* package (Rigaku – Oxford Diffraction 2019). The final intensity data were processed

236   with the *E-STATISTICS* program (implemented in the *WinGX* package, Farrugia 1999), and the

237   statistics of distributions of the normalized structure factors suggested that the structure of inderborite

238   is centrosymmetric (at >70% likelihood). Additional details are given in the CIF (deposited as

239   supplementary material).

240   Low-temperature neutron diffraction data were collected on the four-circle diffractometer D9

241   at the Institut Laue-Langevin (ILL), Grenoble, France, using a single crystal of inderborite of 2.1 x

242   1.8 x 0.9 mm^3. The crystal was glued on an Al pin and placed on a close-circuit displex device

243   operated at 20(1) K (Archer and Lehmann 1986). The diffraction experiment was conducted with a

244   wavelength of 0.8348 Å, obtained from a Cu(220) monochromator, and a small two-dimensional area

245   detector. The data collection strategy was based on a series of ω-scans (for low-Q reflections) or ω-

246   2θ scans (for high-Q reflections), varying the ω-range as a function of the instrument resolution curve.

247   A total of 4732 Bragg reflections was collected up to $2\theta_{max}$ of 114.9° (with $-20 \leq h \leq +19$, $0 \leq k \leq$

248    $+14$ and $-4 \leq l \leq +25$), with $d_{min} = 0.498$ Å; 4509 reflections were unique for symmetry ($R_{int} = 0.0304$,

249   Laue class $2/m$) and 3861 with $I_o > 2\sigma(I_o)$. Integrated intensities, corrected for Lorentz effects, were

250   obtained with the *Racer* program (written by Clive Wilkinson and Garry McIntyre, ILL integration

251   program suite). Absorption correction was also applied, considering the shape of the crystal and its

252   chemical composition, using the ILL program *Datap* (last version of this program is available in the

253   online SXtalSoft repository, https://forge.ill.fr/projects/sxtalsoft/files). The unit-cell was found to be

254   metrically monoclinic, with $a = 12.047(2)$, $b = 7.399(1)$, $c = 19.157(3)$ Å, $\beta = 90.76(1)°$ and $V =$

255   1707.4(6) Å^3, and the reflection conditions consistent with the space group $C2/c$, confirming the

256   previous findings based on the X-ray data. Additional details are given in the CIF (deposited as

257   supplementary material).

258   Two independent crystal-structure refinements were then performed on the basis of the X-ray

259   (at 293 K) and neutron (at 20 K) intensity data, using the SHELXL-2018/3 software (Sheldrick 1997,

260   2008). Neutral X-ray scattering factors (from the *International Tables for X-ray Crystallography -*

261   *Vol. C*) of Mg, Ca, B, O and H were used for the X-ray refinement, whereas their neutron scattering

8

262 lengths were taken from Sears (1986). The secondary isotropic extinction effect was corrected

263 adopting the Larson's formalism (Larson 1967), in both the refinements. The refinements were

264 conducted with the starting structural model reported by Burns and Hawthorne (1994), without any

265 H site. The first cycles of refinement were conducted with isotropic displacement parameters, and

266 then anisotropic, till the convergence was achieved. However, due to the low temperature, the

267 displacement parameters of the B sites in the neutron refinement were modest and quasi-isotropic;

268 they were then modelled as isotropic in the next cycles. When convergence was achieved for both the

269 data set (*i.e.*, neutron and X-ray), a series of residual peaks was found in the final difference-Fourier

270 map of the nuclear or electron density: negative for the neutron refinement, positive for the X-ray

271 one. As H has a negative neutron scattering length (*i.e.*, $b_C(H) = -3.7409$ fm), the negative residual

272 peaks observed in the difference-Fourier map of the nuclear density were assigned to the H sites for

273 the next cycles of refinement. Eleven independent H sites were located, with realistic H-bonding

274 geometry (in terms of O_D-H distances, O_D-H…O_A angles and O_D…O_A distances). Once all the H sites

275 were modelled on the basis of the neutron data, the H population was then implemented in the X-ray

276 refinement. Whereas the H sites were modelled with anisotropic displacement schemes in the neutron

277 refinement, the H population was modelled with a unique isotropic displacement parameter in the X-

278 ray one. When convergence was achieved for both the refinements, the variance-covariance matrix

279 showed no significant correlation among the refined parameters, all the principal mean-square atomic

280 displacement parameters were positive (including those for the H sites for the neutron refinement)

281 and the residuals in the difference-Fourier maps (of nuclear or electron density) were not significant.

282 The final $R_1(F)$ was 0.0695 (for 3861 obs./ 223 par.) for the neutron refinement and 0.0287 (for 1832

283 obs./ 173 par.) for the X-ray one. Some of the final atomic displacement ellipsoids of the neutron

284 structure refinement at 20 K are significantly anisotropic, likely for the not adequate correction of the

285 extinction effects with the isotropic model of Larson (1967). Additional details of the structure

286 refinements are listed in the CIF; relevant interatomic distances and angles are in Table 2.

287

288 **Discussion and implications**

289 The results of the multi-methodological approach used in this study confirm the general

290 formula of inderborite previously reported in the literature: $CaMg[B_3O_3(OH)_5]_2 \cdot 6H_2O$. However,

291 based on the structural model, the correct form of the chemical formula of inderborite should be given

292 as: $CaMg[B_3O_3(OH)_5]_2(H_2O)_4 \cdot 2H_2O$. The chemical analysis here performed showed that there are not

293 major substituents of Ca, Mg or B (Table 1), so that the real chemical composition of the inderborite

294 from Inder is virtually identical to the ideal one, and the concentration of industrially critical elements

295   (*e.g.*, Li, Be or REE) in inderborite is irrelevant (Table 1). The chemical purity of inderborite confirms

296   the previous experimental findings on other hydrous borates, recently re-investigated using modern

297   analytical   protocols   for   the   chemical   characterization.   More   specifically,   colemanite

298   ($Ca[B_3O_4(OH)_3] \cdot H_2O$, Lotti et al. 2017, 2018, 2019), kurnakovite ($Mg[B_3O_3(OH)_5] \cdot 5H_2O$, Gatta et

299   al. 2019), kernite ($Na_6[B_4O_5(OH)_4]_3 \cdot 8H_2O$, Gatta et al. 2020), meyerhofferite ($Ca_2B_6O_6(OH)_{10} \cdot 2H_2O$,

300   Gatta et al. 2022a) and also probertite ($CaNa[B_5O_7(OH)_4] \cdot 3H_2O$, Gatta et al. 2022b) show no

301   significant concentration of isomorphic substituents of the principal elements; as a result, their

302   experimental formulae are basically identical to the ideal ones. The chemical purity of the hydrous

303   borates was already reported as a common feature of this mineral population that does not depend on

304   the nature of the deposit (*e.g.*, Gatta et al. 2019, 2020, 2022b), but appears to be rather governed by

305   the crystal structure selectivity and, likely, it is also the results of iterated dissolution and

306   recrystallization in lacustrine environments, which could promote purification. The *in-situ* B isotopic

307   composition of the Inder inderborite is relatively homogeneous and significantly enriched in the ^{11}B

308   isotope. As observed in this study, single spot analyses along a rim-core-rim profile parallel to the *c*-

309   axis report identical B isotope composition within error (from +34.89 ± 0.53 to +35.61 ± 0.66 %;

310   error expressed as 2σ), thus providing a weighted mean $\delta^{11}B$ of +35.15 ± 0.49‰ (2σ, N = 6) (Table

311   1). Such a $\delta^{11}B$ value falls within the range of values in which the source of boron is ascribable to

312   marine reservoirs, rather than to terrestrial ones (*e.g.*, Swihart and Moore 1986, Hussain et al. 2021,

313   and references therein). At the Inder deposits, the borates occur as veins at the top of a large salt dome

314   complex, and are considered as the effect of remobilization and concentration during the intrusion of

315   the salt dome itself (Helvaci 2005).

316   The X-ray and neutron structure refinements of this study consistently confirm the general

317   structural model of inderborite previously reported by Burns and Hawthorne (1994). The principal

318   building block unit of the structure is a $[B_3O_3(OH)_5]^{2-}$ ring, usually represented by the descriptor <Δ2□>

319   (where Δ stands for a $B\varphi_3$ unit and □ for a $B\varphi_4$ tetrahedron; φ is O^{2-}, OH^- or H_2O, Burns et al. 1995,

320   Hawthorne 2012) or 3:1Δ+2*T* (Christ and Clark 1977), consisting of 2$B\varphi_4$ tetrahedra (*i.e.*, $BO_2(OH)_2$,

321   B-ion in sp^3 electronic configuration) and one planar-triangular $B\varphi_3$ group (*i.e.,* BO_2OH, B-ion in sp^2

322   electronic configuration) (Fig. 1, Table 2). In the $[B_3O_3(OH)_5]^{2-}$ ring, all the oxygen atoms that are not

323   shared between two boron atoms are protonated. The building units share corners with the $Ca\varphi_8$

324   polyhedra (*i.e.*, antiprism $CaO_2(OH)_4(OH_2)_2$) and $Mg\varphi_6$ octahedra (*i.e.*, $Mg(OH)_4(OH_2)_2$), forming

325   hetero-polyhedral sheets parallel to (100), as shown in Fig. 1. Subsequent hetero-polyhedral sheets are

326   mutually connected only by H-bonding interactions, even mediated by the zeolitic (*i.e.*, "interstitial")

327   H_2O molecules. This structural feature occurs even in other hydrous borates, *e.g.* in kurnakovite (Gatta

328   et al. 2019), and well explains the good cleavage on {100} usually observed in inderborite crystals.

329   A careful analysis of the X-ray and neutron structural models obtained in this study shows that

330   (numerical data from the neutron refinement):

331   1) The unique triangular group (*i.e.*, $B3O_2OH$) exhibits an almost ideal configuration, with

332       $\Delta(B3\text{-}O)_{max} \sim 0.02$ Å (*i.e.*, where Δ is the difference between the longest and the shortest B-

333   O refined distances), average O-B-O angles of 120° (ranging between 116.2°-123.8°) and

334   aplanarity < 0.9° (here defined as the average angle described by the plane on which the 3-

335   oxygen sites lie and each of the three independent $B\text{-}O_n$ vectors) (CIF, Table 2). The two

336   independent tetrahedral units (*i.e.*, $B1O_2(OH)_2$ and $B2O_2(OH)_2$; Fig. 2, Table 2) are slightly

337   distorted, with: $\Delta(B1\text{-}O)_{max} \sim 0.05$ Å, $<O\text{-}B1\text{-}O> \sim 109.5°$ and $\Delta(O\text{-}B1\text{-}O)_{max} \sim 5.3°$; $\Delta(B2\text{-}$

338       $O)_{max} \sim 0.06$ Å, $<O\text{-}B2\text{-}O> \sim 109.5°$ and $\Delta(O\text{-}B2\text{-}O)_{max} \sim 4.3°$. The longest distances (*i.e.*,

339   B1-O2 and B2-O8) are ascribable to the B-OH bonds (CIF, Table 2).

340   2) The Mg-octahedron, in which Mg^{2+} is coordinated by four hydroxyl groups and two H_2O

341   molecules (*i.e.*, $Mg(OH)_4(OH_2)_2$), is only slightly distorted, with $\Delta(Mg\text{-}O)_{max} \sim 0.04$ Å,

342       $<O\text{-}Mg\text{-}O> = 90.0°$ (ranging between 86.1°-93.9°) and $\Delta(O\text{-}Mg\text{-}O)_{max} \sim 5.2°$. As expected,

343   the Ca-polyhedron (in an antiprism configuration), in which the cation is coordinated by

344   two O, four OH-groups and two H_2O molecules (*i.e.*, $CaO_2(OH)_4(OH_2)_2$), is significantly

345   distorted with $Ca\text{-}O_{min} \sim 2.38$ and $Ca\text{-}O_{max} \sim 2.48$ Å (Figs. 1 and 2, CIF, Table 2).

346   3) In the structure of inderborite, three crystallographically independent H_2O molecule sites

347   occur: H6-O9-H7 (bonded to Mg), H8-O10-H9 (bonded to Ca) and H10-O11-H11 (the

348   "zeolitic" molecule) (Table 2). All the refined O-H bond distances were corrected for the

349   "riding motion effect", following the protocol of Busing and Levy (1964), with final

350   distances ranging between 0.990 and 1.003 Å (Table 2). Two among the independent H_2O

351   molecules show an almost ideal geometrical configuration, with H6-O9-H7 = 105.5(3)° and

352   H10-O11-H11 = 106.1(3)°, whereas the third one shows a "stretched" configuration with

353   H8-O10-H9 = 109.4(3)°. The H-bonding scheme of the three H_2O molecules is the

354   following:

355   -   for H6-O9-H7, the *acceptors* are the oxygen sites O10 and O11, with O9-H6...O10 =

356   167.0(3)° (O9...O10 = 2.760(2) Å) and O9-H7...O11 = 166.2(3)° (O9...O11 = 2.811(2)

357   Å);

11

358 - for H8-O10-H9, the *acceptors* are the oxygen sites O4 and O5, with O10-H8...O4 =

359 168.1(2)° (O10...O4 = 2.770(2) Å) and O10-H9...O5 = 154.2(2)° (O10...O5 = 2.723(1)

360 Å);

361 - for H10-O11-H11, the H-bonding scheme is more complex, with a bifurcated

362 configurations for H10: the *acceptors* are the oxygen sites O6 and O9 (*via* H10), and O8

363 (*via* H11), with O11-H10...O6 = 125.0(3)° (O11...O6 = 3.141(2) Å), O11-H10…O9 =

364 136.4(3)° (O11…O9 = 2.271(4) Å), and O11-H11...O8 = 159.8(3)° (O11...O8 = 2.857(2)

365 Å) (Fig. 2, Table 2).

366 Excluding the bifurcated H-bond of the zeolitic H_2O molecule, mediated by the H10 proton,

367 (*i.e.*, O11-H10...O6 and O11-H10…O9), all the other O_D-H…O_A angles range between 154°

368 and 168°, with O_D…O_A distances between 2.72 and 2.86 Å, approaching a configuration

369 energetically favourable (Table 2). The bifurcated configuration of the H-bonding scheme

370 mediated by H10 is the only possible, considering all the potential acceptor sites with O_D…O_A

371 and H…O_A distances compatible for a potential H-bond interaction.

372 The "stretched" configuration of the H8-O10-H9 molecule is the effect of the location of the

373 two acceptor sites: O4 and O5 describe, along with the donor O10, a significantly obtuse

374 O4…O10…O5 angle of about 120.8°, forcing the H8-O10-H9 molecule to have a H-O-H

375 angle of about 109.4° in order to keep the O4…H8-O10-H9…O5 bonding scheme (Fig. 2).

376 Often, in minerals, the H-O-H geometry tends to deviate from the ideal configuration in

377 response to the H-bonding environment, forcing the molecules to have "compressed" or

378 "stretched" forms (*e.g.,* Gatta et al. 2008, 2021).

379 The hydroxyl groups (*i.e.*, O2-H, O3-H, O6-H, O7-H, and O8-H, CIF and Table 2), in the

380 structure of inderborite, show O-H distances, corrected for "riding motion effect", ranging

381 between 0.98-1.01 Å, O_D...O_A distances between 2.62-3.22 Å, and O_D-H...O_A angles between

382 141-169°.

383 Overall, 10 over 11 independent oxygen sites in the structure of inderborite are involved in H-

384 bonds as *donor* or *acceptors* (Table 2), and this reflects the pervasive effect of the H-bonding

385 network. According to Burns and Hawthorne (1994), the role played by the complex H-bond

386 network is expected to be substantial on the stability of the crystalline edifice, having effects

387 within the single hetero-polyhedral sheet (*i.e.*, O7-H4...O3, O9-H6...O10 and O10-H9...O5, Fig.

388 2, Table 2), between subsequent sheets (*i.e.*, O3-H2...O7, O6-H3...O7 and O10-H8...O4, Fig. 2,

389 Table 2), and to bond the interstitial zeolitic H_2O molecules (*i.e.*, O11-H10...O9, O11-H10...O6,

390 and O11-H11...O8, Fig. 2, Table 2). It is worth to note that the atomic positions of the H sites

12

391   obtained in this study by neutron diffraction are similar, but not identical, to those reported by

392   Burns and Hawthorne (1994), who were even forced to impose soft constraints to the O-H

393   distances (*i.e.*, 0.96 Å) in their structure refinement. As a result, the geometry of the H_2O

394   molecules is different: for example, our neutron refinement provides the H6-O9-H7 angle of

395   105.4(3)° (Table 2), whereas the counterpart based on the X-ray refinement of Burns and

396   Hawthorne (1994) is 100(3)°. A similar limitation, concerning the location of the H sites, is

397   also in the X-ray structural model of this study based on the use of a modern device. This

398   further supports the important role of the neutron diffraction to provide better structural

399   models of hydrous materials, if compared to the X-ray ones, especially when a complex and

400   pervasive H-bonding network occurs into the crystalline edifice.

401   4) The Raman spectrum of inderborite reported in the RRUFF database

402   (https://rruff.info/Inderborite) and in collection of Chukanov (2014), shows at least seven

403   independent peaks in the O-H stretching region (*i.e.*, 3000-3700 cm^{-1}). This finding supports

404   the complex H-bonding scheme described in this study.

405   The experimental findings about the complex and pervasive nature of the H-bonding scheme in

406   inderborite confirm the previous results for other hydrous borates (*e.g.*, Lotti et al. 2018, 2019; Gatta

407   et al. 2019, 2020, 2022a, 2002b). We expect that a thermal, compressional or chemical perturbation

408   of the H-bonding scheme would easily lead to a phase transition, or even to a decomposition of this

409   mineral. At present, the behaviour of inderborite at non-ambient conditions is entirely unknown.

410   In the framework of a long-term project on the potential utilization of natural borates as B-rich

411   aggregates in concretes, acting as radiation-shielding materials for the pronounced ability of ^{10}B to

412   absorb thermal neutrons, we have recently reinvestigated the high/low-temperature and high-pressure

413   crystal-chemistry of a series of hydrous borates, bracketing their phase stability fields and the

414   potential destabilization factors governed by the crystal structure (*e.g.*, Lotti et al. 2017, 2018,

415   Pagliaro et al. 2021, Comboni et al. 2020a, 2020b, 2022, 2023). Inderborite, with its high B-content

416   (*ca.* 41 wt% B_2O_3) could potentially be a good candidate as a B-rich aggregate in concretes. To the

417   best of our knowledge, the solubility and the effects in the hardening stage of inderborite in Portland

418   or in Sorel cement pastes is still unknown. Inderborite does not contain the alkali elements, *i.e.*, Na

419   or K, which could potentially generate the so-called "alkali-silica reactions" – ASR, deleterious for

420   the durability of Portland cements.

421

422

423

424
425
426
427
428
429
430
431
432
433
434
435
436

14

References

437   Archer, J. and Lehmann, M.S. (1986) A simple adjustable mount for a two-stage
439   cryorefrigerator on an Eulerian cradle. Journal of Applied Crystallography, 19, 456-459.

440   Burns, P.C. and Hawthorne, F.C. (1994) Structure and hydrogen bonding in inderborite, a
441   heteropolyhedral sheet structure. The Canadian Mineralogist, 32, 533-539.

442   Burns, P.C., Grice, J.D., and Hawthorne, F.C. (1995) Borate minerals; I, Polyhedral clusters and
443   fundamental building blocks. The Canadian Mineralogist, 33, 1131–1151.

444   Busing, W.R. and Levy, H.A. (1964) The effect of thermal motion on the estimation of bond
445   lengths from diffraction measurements. Acta Crystallographica, 17, 142-146.

446   Carter, R.S., Palevsky, H., Myers, V.W., and Hughes, D.J. (1953) Thermal neutron absorption
447   cross sections of boron and gold. Physical Review, 96, 716-721.

448   Catanzaro, F., Champion, C., Garner, E., Marinenko, G., Sappenfield, K., and Shields, W.
449   (1970) Boric acid: isotopic and assay standard reference materials. National Bureau of Standards
450   Special Publication, 260, 1–70.

451   Christ, C.L. and Clark, J.R. (1977) A crystal-chemical classification of borate structures with
452   emphasis on hydrated borates. Physics and Chemistry of Minerals, 2, 59-87.

453   Chukanov, N.V. (2014) Infrared spectra of mineral species: Extended library. Springer
454   (Springer Geochemistry/Mineralogy), vol. 1, Dordrecht, 1726 pp.

455   Comboni, D., Pagliaro, F., Gatta, G.D., Lotti, P., Milani, S., Merlini, M., Battiston, T.,
456   Glazyrin, K., and Liermann, H.-P. (2020a) High-pressure behavior and phase stability of
457    $Na_2B_4O_6(OH)_2 \cdot 3H_2O$ (kernite). Journal of the American Ceramic Society, 103, 5291–5301.

458   Comboni, D., Pagliaro, F., Gatta, G.D., Lotti, P., Battiston, T., Garbarino, G., and Hanfland,
459   M. (2020b) High-pressure behaviour and phase stability of $Ca_2B_6O_6(OH)_{10} \cdot 2(H_2O)$ (meyerhofferite).
460   Physics and Chemistry of Minerals, 47, 50.

461   Comboni, D., Battiston, T., Pagliaro, F., Lotti, P., Gatta, G.D., and Hanfland, M. (2022) High-
462   pressure behaviour and atomic-scale deformation mechanisms in inyoite, $CaB_3O_3(OH)_5 \cdot 4H_2O$.
463   Physics and Chemistry of Minerals, 49, 4.

464   Comboni, D., Poreba, T., Battiston, T., Hanfland, M., and Gatta, G.D. (2023) On the
465   anomalous high-pressure phase transition of inderite, $MgB_3O_3(OH)_5 \cdot 5H_2O$. Solid State Sciences,
466   140, 107187.

467   Farrugia, L.J. (1999) WinGX suite for small-molecule single-crystal crystallography. Journal
468   of Applied Crystallography, 32, 837-838.

469   Fleischer, M. (1943) New mineral names. American Mineralogist, 28, 282-284.

Gatta, G.D., Rotiroti, N., McIntyre, G.J., Guastoni, A., and Nestola, F. (2008) New insights into the crystal chemistry of epididymite and eudidymite from Malosa, Malawi: a single-crystal neutron diffraction study. American Mineralogist, 93, 1158-1165.

Gatta, G.D., Guastoni, A., Lotti, P., Guastella, G., Fabelo, O., and Fernandez-Diaz, M.T. (2019) A multi-methodological study of kurnakovite: A potential B-rich aggregate. American Mineralogist, 104, 1315-1322.

Gatta, G.D., Guastoni, A., Lotti, P., Guastella, G., Fabelo, O., and Fernandez-Diaz, M.T. (2020) A multi-methodological study of kernite, a mineral commodity of boron. American Mineralogist, 105, 1424–1431.

Gatta, G.D., Hradil, K., and Meven, M. (2021) Where is the Hydrogen? Elements, 17, 163-168

Gatta, G.D., Guastella, G., Capelli, S., Comboni, D., and Guastoni, A. (2022a) On the crystal-chemistry of meyerhofferite, $CaB_3O_6(OH)_5 \cdot H_2O$. Physics and Chemistry of Minerals, 49, 22.

Gatta, G.D., Cannaò, E., Gagliardi, V., and Fabello, O. (2022b) Reinvestigation of probertite, $CaNa[B_5O_7(OH)_4] \cdot 3H_2O$, a mineral commodity of boron. American Mineralogist, 107, 1378–1384.

Gorshkov, G.S. (1941) A new mineral from the region of Lake Inder. Comptes Rendus (Doklady) de l'Académie des Sciences de l'URSS, 33, 254-256.

Griffin, W.L., Powell, W.., Pearson, N.J., and O'reilly, S.Y. (2008) *GLITTER*: data reduction software for laser ablation ICP-MS. Laser Ablation-ICP-MS in the Earth Sciences: Current practices and outstanding issues, 308-311. Mineralogical Association of Canada.

Hawthorne, F.C. (2012) A bond-topological approach to theoretical mineralogy: crystal structure, chemical composition and chemical reactions. Physics and Chemistry of Minerals, 39, 841–874.

Helvaci, C. (2005) Borates. In: Selley RC, Cocks LRM and Plimer IR (Eds), Encyclopedia of Geology. Elsevier, 3, 510-522.

Hussain, S.A., Han, F.Q., Ma, Z., Hussain, A., Mughal, M.S., Han, J., Alhassan, A., Widory, D. (2021) Unraveling Sources and Climate Conditions Prevailing during the Deposition of Neoproterozoic Evaporites Using Coupled Chemistry and Boron Isotope Compositions ($\delta^{11}B$): The Example of the Salt Range, Punjab, Pakistan. Minerals, 11, 161.

Ikornikova, M.V. and Godlevsky, M.N. (1941) The new borate: metahydroboracite. Comptes rendus de l'académie des sciences de l'U.R.S.S., 33, 257-258.

Jochum, K.P., Weis, U., Stoll, B., Kuzmin, D., Yang, Q., Raczek, I., Jacob, D.E., Stracke, A., Birbaum, K., Frick, D.A., and others (2011) Determination of reference values for NIST SRM 610-617 glasses following ISO guidelines. Geostandards and Geoanalytical Research, 35, 397–429.

16

503

504   Kurkutova, E., Rumanova, I., and Belov, N. (2023) Crystal Structure of Inderborite. Soviet

505   Physics-Doklady, 10, 808-810.

506   Larson, A.C. (1967) Inclusion of secondary extinction in least-squares calculations. Acta

507   Crystallographica, 23, 664-665.

508   Leeman, W.P., and Tonarini, S. (2001) Boron Isotopic Analysis of Proposed Borosilicate

509   Mineral Reference Samples. Geostandards and Geoanalytical Research, 25, 399–403.

510   Lotti, P., Gatta, G.D., Comboni, D., Guastella, G., Merlini, M., Guastoni, A., and Liermann, H.P.

511   (2017) High-pressure behavior and P-induced phase transition of $CaB_3O_4(OH)_3 \cdot H_2O$ (colemanite).

512   Journal of American Ceramic Society, 100, 2209-2220.

513   Lotti, P., Gatta, G.D., Demitri, N., Guastella, G., Rizzato, S., Ortenzi, M.A., Magrini, F.,

514   Comboni, D., Guastoni, A., and Fernandez-Diaz, M.T. (2018) Crystal-chemistry and temperature

515   behavior of the natural hydrous borate colemanite, a mineral commodity of boron. Physics and

516   Chemistry of Minerals, 45, 405-422.

517   Lotti, P., Comboni, D., Gigli, L., Carlucci, L., Mossini, E., Macerata, E., Mariani, M., and Gatta,

518   G.D. (2019) Thermal stability and high-temperature behavior of the natural borate colemanite: An

519   aggregate in radiation-shielding concretes. Construction and Building Materials, 203, 679–686.

520   Marger, K., Harlaux, M., Rielli, A., Baumgartner, L.P., Dini, A., Dutrow, B.L., and Bouvier,

521   A.S. (2020) Development and Re-Evaluation of Tourmaline Reference Materials for In Situ

522   Measurement of Boron δ Values by Secondary Ion Mass Spectrometry. Geostandards and Geoanalytical

523   Research, 44, 593–615.

524   Marschall, H.R., Ludwig, T., Altherr, R., Kalt, A., and Tonarini, S. (2006) Syros metasomatic

525   tourmaline: Evidence for very high-$\delta^{11}B$ fluids in subduction zones. Journal of Petrology, 47, 1915–

526   1942.

527   Míková, J., Košler, J., and Wiedenbeck, M. (2014) Matrix effects during laser ablation MC

528   ICP-MS analysis of boron isotopes in tourmaline. Journal of Analytical Atomic Spectrometry, 29,

529   903–914.

530   Pagliaro, F., Lotti, P., Battiston, T., Comboni, D., Gatta, G.D., Cámara, F., Milani, S., Merlini,

531   M., Glazyrin, K., and Liermann, H-P. (2021) Thermal and compressional behavior of the natural borate

532   kurnakovite, $MgB_3O_3(OH)_5 \cdot 5H_2O$. Construction and Building Materials, 266, 121094.

533   Palmer, M.R. and Swihart, G.H. (1996) Boron Isotope Geochemistry: An Overview. In L.M.

534   Anovitz, E.S. Grew (Eds.), Boron: Mineralogy, Petrology, and Geochemistry, Review in Mineralogy

535   33, Mineralogical Society of America, Chantilly, pp. 709-744.

536   Pekov, I.V. (1998) Minerals First discovered on the territory of the former Soviet Union. Ocean
537 Pictures, Moscow, 369 p.

538   Pekov, I.V. and Abramov, D.V. (1993) Boron deposit of the Inder and its minerals. World of
539 Stones, 1, 23-30.

540   Rauch, H., and Waschkowski, W. (2002) Neutron Scattering Lengths. In A.J. Dianoux, G.
541 Lander (Eds.), Neutron Data Booklet, first ed., Institut Laue Langevin, Grenoble, pp. 1-18.

542   Rigaku-Oxford Diffraction (2019) *CrysAlisPro*: Single Crystal X-ray diffraction data collection
543 and processing software. Rigaku Corporation (www.rigaku.com/products/crystallography/crysalis).

544   Sears, V.F. (1986) Neutron Scattering Lengths and Cross-Sections. In K. Sköld and D.L.
545 Price, Eds., Neutron Scattering, Methods of Experimental Physics, Vol. 23A, Academic Press, New
546 York, pp. 521-550.

547   Sheldrick, G.M. (1997) SHELXL-97. Programs for crystal structure determination and
548 refinement. University of Göttingen, Germany.

549   Sheldrick, G.M. (2008) A short history of SHELX. Acta Crystallographica, A64, 112-122.

550   Swihart, G.H. and Moore, P.B. (1986) Boron isotopic composition of marine and nonmarine
551 evaporite borates. Geochimica and Cosmochimica Acta, 50, 1297–1301.

552   Tonarini, S., Pennisi, M., Adorni-braccesi, A., Dini, A., Ferrara, G., Gonfiantini, R., Wiedenbeck,
553 M., and Gröning, M. (2003) Intercomparison of Boron Isotope and Concentration Measurements. Part
554 I : Selection, Preparation and Homogeneity Tests of the Intercomparison Materials. Geostandards
555 Newsletter, 27, 21–39.

556   Wilson, S.A. (2018) G-probe 20 summary report: International Association of Geoanalysts G-
557 probe 20, 1–13 p.

558   Wu, S., Yang, Y., Jochum, K.P., Romer, R.L., Glodny, J., Savov, I.P., Agostini, S., De Hoog,
559 J.C.M., Peters, S.T.M., Kronz, A., and others (2021) Isotopic Compositions (Li-B-Si-O-Mg-Sr-Nd-Hf-
560 Pb) and Fe2+/ΣFe Ratios of Three Synthetic Andesite Glass Reference Materials (ARM-1, ARM-2,
561 ARM-3). Geostandards and Geoanalytical Research, 45, 719–745.

562

563

564

565

566

567

568 Table 1. Trace element concentrations (in wt ppm, 1σ) and B isotope composition (in ‰, 2σ) of
569 inderborite, based on the LA-ICP-MS and LA-MC-ICP-MS data.
570

Analyzed isotope	Analyte symbol	Average (N = 6)	1σ
7	Li	<13.5	
9	Be	2.85	1.36
45	Sc	<9.97	
49	Ti	<29.53	
51	V	<3.31	
53	Cr	<52.37	
55	Mn	<8.05	
59	Co	<8.02	
60	Ni	<34.14	
65	Cu	<42.83	
66	Zn	<36.57	
75	As	21.1	6.4
85	Rb	<3.80	
88	Sr	35.6	43.4
89	Y	<0.25	
90	Zr	<0.38	
93	Nb	<0.64	
111	Cd	2.34	1.37
121	Sb	<2.55	
133	Cs	<1.21	
137	Ba	0.997	0.806
139	La	0.143	0.046
140	Ce	0.390	0.028
141	Pr	0.061	0.017
146	Nd	1.14	0.82
149	Sm	0.700	0.710
151	Eu	0.190	0.190
157	Gd	0.465	0.092
159	Tb	0.124	0.049
163	Dy	<0.001	
165	Ho	0.060	0.060
167	Er	<0.55	
169	Tm	0.037	0.077
173	Yb	<0.001	
175	Lu	0.078	0.079
177	Hf	<0.001	
181	Ta	0.053	0.035
182	W	0.450	0.410
208	Pb	1.43	0.61
232	Th	<0.001	
238	U	<0.125	

		Weighted mean (N = 6)	2σ
	$\delta^{11}B$	+35.15	0.49

571

572

573

574 Table 2. Principal bond distances (Å) and angles (°) in the structure of inderborite, based on the X-
575 ray refinement (data collected at 293 K) and neutron structure refinement (data collected at 20 K).

576

X-ray data (T = 293 K)					
Mg-O2 (x 2)	2.083(1)	O2-H1	0.93(2)	O10-H8	0.92(2)
Mg-O8 (x 2)	2.106(1)	O2-H1*	0.96	O10-H8*	0.95
Mg-O9 (x 2)	2.092(1)	O2...O11	3.229(2)	O10...O4	2.803(2)
		H1...O11	2.45(2)	H8...O4	1.90(2)
Ca-O1 (x 2)	2.392(1)	O2-H1...O11	141(2)	O10-H8...O4	165(2)
Ca-O3 (x 2)	2.443(1)				
Ca-O6 (x 2)	2.504(1)	O3-H2	0.91(2)	O10-H9	0.93(2)
Ca-O10 (x 2)	2.450(1)	O3-H2*	0.94	O10-H9*	0.96
		O3...O7	2.863(2)	O10...O5	2.727(2)
B1-O1	1.438(2)	H2...O7	2.00(2)	H9...O5	1.85(2)
B1-O2	1.491(2)	O3-H2...O7	158(2)	O10-H9...O5	157(2)
B1-O3	1.477(2)			H8-O10-H9	112(2)
B1-O4	1.483(2)	O6-H3	0.93(2)		
		O6-H3*	0.96	O11-H10	0.93(2)
B2-O1	1.443(2)	O6...O7	2.657(2)	O11-H10*	0.96
B2-O5	1.487(2)	H3...O7	1.74(2)	O11...O9	3.107(2)
B2-O7	1.459(2)	O6-H3...O7	169(2)	H10...O9	2.40(3)
B2-O8	1.504(2)			O11-H10...O9	133(2)
		O7-H4	0.94(2)		
B3-O4	1.360(2)	O7-H4*	0.97	O11...O6	3.166(2)
B3-O5	1.360(2)	O7...O3	2.826(1)	H10...O6	2.48(2)
B3-O6	1.383(2)	H4...O3	1.90(2)	O11-H10...O6	131(2)
		O7-H4...O3	166(2)		
O1-B1-O2	109.1(1)			O11-H11	0.91(2)
O1-B1-O3	107.0(1)	O8-H5	0.92(2)	O11-H11*	0.94
O1-B1-O4	112.2(1)	O8-H5*	0.95	O11...O8	2.918(2)
O2-B1-O3	112.1(1)	O8...O11	2.929(2)	H11...O8	2.06(2)
O2-B1-O4	108.9(1)	H5...O11	2.06(2)	O11-H11...O8	156(2)
O3-B1-O4	107.5(1)	O8-H5...O11	158(2)	H10-O11-H11	102(2)
O1-B2-O5	110.6(1)	O9-H6	0.93(2)		
O1-B2-O7	111.9(1)	O9-H6*	0.96		
O1-B2-O8	109.1(1)	O9...O10	2.774(2)		
O5-B2-O7	108.9(1)	H6...O10	1.86(2)		
O5-B2-O8	107.6(1)	O9-H6...O10	170(2)		
O7-B2-O8	108.6(1)				
		O9-H7	0.93(2)		
O4-B3-O5	123.8(1)	O9-H7*	0.96		
O4-B3-O6	120.0(1)	O9...O11	2.816(2)		
O5-B3-O6	116.2(1)	H7...O11	1.91(2)		
		O9-H7...O11	164(2)		
O2-Mg-O8 (x 2)	86.55(4)	H6-O9-H7	100(2)		
O2-Mg-O8' (x 2)	93.45(4)				
O2-Mg-O9 (x 2)	88.30(5)				
O2-Mg-O9' (x 2)	91.70(5)				
O8-Mg-O9 (x 2)	89.85(5)				
O8-Mg-O9' (x 2)	90.15(5)				

* Bond distance corrected for "riding motion" effect, according to Busing and Levy (1964)

20

618
619
620
621
622
623
624
625
626
627
628
629
630
631
632
633
634
635
636
637
638
639
640
641
642
643
644
645
646
647
648
649
650
651
652
653
654
655
656
657
658
659
660
661
662
663
664
665

Neutron data (T = 20 K)					
Mg-O2 (x 2)	2.072(1)	O2-H1	0.956(3)	O10-H8	0.977(3)
Mg-O8 (x 2)	2.111(1)	O2-H1*	0.985	O10-H8*	0.996
Mg-O9 (x 2)	2.096(1)	O2...O11	3.223(2)	O10...O4	2.770(2)
		H1...O11	2.411(4)	H8...O4	1.807(3)
Ca-O1 (x 2)	2.384(1)	O2-H1...O11	142.6(3)	O10-H8...O4	168.1(2)
Ca-O3 (x 2)	2.439(1)				
Ca-O6 (x 2)	2.485(1)	O3-H2	0.970(2)	O10-H9	0.982(3)
Ca-O10 (x 2)	2.439(1)	O3-H2*	0.988	O10-H9*	0.999
		O3...O7	2.851(1)	O10...O5	2.723(1)
B1-O1	1.438(1)	H2...O7	1.921(3)	H9...O5	1.804(3)
B1-O2	1.492(2)	O3-H2...O7	159.6(2)	O10-H9...O5	154.2(2)
B1-O3	1.474(2)			H8-O10-H9	109.4(3)
B1-O4	1.483(1)	O6-H3	0.993(3)		
		O6-H3*	1.009	O11-H10	0.966(3)
B2-O1	1.439(2)	O6...O7	2.618(2)	O11-H10*	0.992
B2-O5	1.483(1)	H3...O7	1.633(3)	O11...O9	3.044(2)
B2-O7	1.464(1)	O6-H3...O7	170.6(2)	H10...O9	2.271(4)
B2-O8	1.505(2)			O11-H10...O9	136.4(3)
		O7-H4	0.975(3)		
B3-O4	1.362(1)	O7-H4*	0.993	O11...O6	3.141(2)
B3-O5	1.359(1)	O7...O3	2.779(2)	H10...O6	2.485(4)
B3-O6	1.383(1)	H4...O3	1.817(3)	O11-H10...O6	125.0(3)
		O7-H4...O3	168.5(3)		
O1-B1-O2	109.1(1)			O11-H11	0.970(4)
O1-B1-O3	106.74(9)	O8-H5	0.970(3)	O11-H11*	0.992
O1-B1-O4	112.08(8)	O8-H5*	0.987	O11...O8	2.857(2)
O2-B1-O3	111.90(8)	O8...O11	2.917(2)	H11...O8	1.928(3)
O2-B1-O4	108.99(8)	H5...O11	1.976(3)	O11-H11...O8	159.8(3)
O3-B1-O4	108.1(1)	O8-H5...O11	162.8(2)	H10-O11-H11	106.1(3)
O1-B2-O5	111.3(1)	O9-H6	0.986(3)		
O1-B2-O7	111.41(9)	O9-H6*	1.003		
O1-B2-O8	108.78(8)	O9...O10	2.760(2)		
O5-B2-O7	108.66(8)	H6...O10	1.790(3)		
O5-B2-O8	107.59(9)	O9-H6...O10	167.0(3)		
O7-B2-O8	109.0(1)				
		O9-H7	0.973(3)		
O4-B3-O5	123.20(9)	O9-H7*	0.990		
O4-B3-O6	120.3(1)	O9...O11	2.811(2)		
O5-B3-O6	116.45(9)	H7...O11	1.857(3)		
		O9-H7...O11	166.2(3)		
O2-Mg-O8 (x 2)	86.10(4)	H6-O9-H7	105.4(3)		
O2-Mg-O8' (x 2)	93.90(4)				
O2-Mg-O9 (x 2)	87.57(5)				
O2-Mg-O9' (x 2)	92.43(5)				
O8-Mg-O9 (x 2)	89.58(4)				
O8-Mg-O9' (x 2)	90.42(4)				

* Bond distance corrected for "riding motion" effect, according to Busing and Levy (1964)

666 Figure 1 (*Color*). The principal building block unit (made by the $[B_3O_3(OH)_5]^{2-}$ ring), a fragment of
667 the hetero-polyhedral sheets parallel to (100) (made by the building block units connected to Ca- and
668 Mg-polyhedra) and a view down [010] of the crystal structure of inderborite. Structure model based
669 on the neutron structure refinement of this study (intensity data collected at 20 K). Displacement
670 ellipsoid probability factor: 90%. Atomic site labels in Fig. 2.

671
672
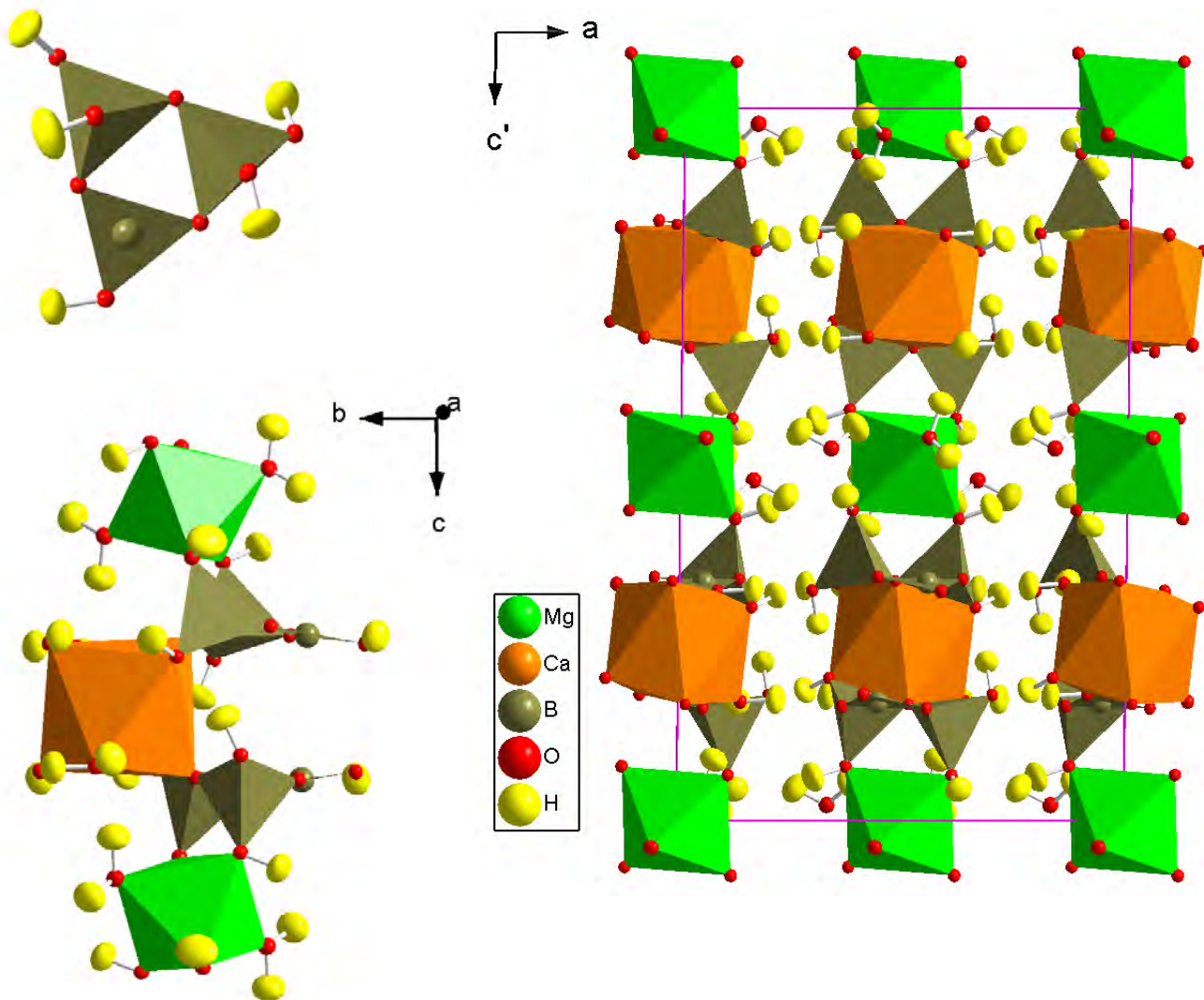
673
674
675
676
677
678
679
680
681
682
683
684

22

Figure 2 (*Color*). The complex and pervasive H-bonding scheme into the crystal structure of inderborite, based on the neutron structure refinement of this study (data collected at 20 K). Details in Table 2. Displacement ellipsoid probability factor: 90%.